ARTICLE

Quantitative Determination of Metal Ion Adsorption on Cellulose Nanocrystals Surfaces

Harrison R. Paul, Mrinal K. Bera, Nicholas Macke, Stuart J. Rowan,* and Matthew V. Tirrell*

Read Online

ACCESS | Metrics & More | Article Recommendations | SI Supporting Information

ABSTRACT: Nanocellulose is a bio-based material that holds significant potential in the field of water purification. Of particular interest is their potential use as a key sorbent material for the removal of metal ions from solution. However, the structure of metal ions adsorbed onto cellulose surfaces is not well understood. The focus of this work is to determine quantitatively the three-dimensional distribution of metal ions of different valencies surrounding negatively charged carboxylate functionalized cellulose nanocrystals (CNCs) using anomalous small-angle X-ray scattering (ASAXS). These distributions can affect the water and ionic permeability in these materials. The data show that increasing the carboxylate density on the surface of the CNCs from 740 to 1100 mmol/kg changed the nature of the structure of the adsorbed ions from a monolayer into a multilayer structure. The monolayer was modeled as a Stern layer around the CNC nanoparticles, whereas the multilayer structure was modeled as a diffuse layer on top of the Stern layer around the nanoparticles. Within the Stern layer, the maximum ion density increases from 1680 to 4350 mmol of Rb^+/(kg of CNC) with the increase in the carboxylate density on the surface of the nanoparticles. Additionally, the data show that CNCs can leverage multiple mechanisms, such as electrostatic attraction and the chaotropic effect, to adsorb ions of different valencies. By understanding the spatial organization of the adsorbed metal ions, the design of cellulose-based sorbents can be further optimized to improve the uptake capacity and selectivity in separation applications.
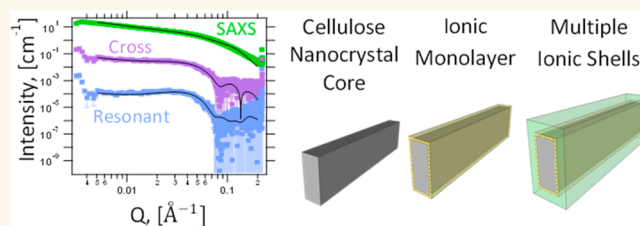
KEYWORDS: Cellulose Nanocrystals, Adsorption, Anomalous Small Angle X-ray Scattering, Sorbents, Water Purification, Ion Exchange

As the needs for water in industrial processes, for agriculture, and for personal consumption continue to increase and natural reservoirs are strained, more regions are becoming water-stressed such that the demand for water in these regions has (or soon will) exceed the available water. Increased urbanization in these water-stressed regions coupled with industrial expansion increases the demand for these limited water sources.[1,2] Additionally, pollution from dyes,[3] heavy metals, and pesticides[4] is a growing problem that threatens the supply of fresh water.[5,6] Dye effluents have been identified as the largest class of pollutants from industrial sources and are especially problematic as they pose health risks to humans, flora, and fauna.[3,6−8] In addition to dye contamination, heavy metal pollution is a growing ecological and public health concern.[9,10] Heavy metals can have deleterious effects even at extremely low concentrations; therefore, effective removal methods are essential to producing safe, potable water.

This demand, coupled with the declining supply, heightens the need for potable water to be produced from underutilized resources, such as contaminated fresh water and wastewater. For example, according to the U.S. Environmental Protection Agency (EPA), only 7−8% of the 32 billion gallons of waste

effluent produced each day are recycled.[11] To improve this, several technologies like membrane filtration, flocculation, and sorbents are used to generate potable water.[6] Of these methods, sorbents are commonly used to remove contaminants that are not easily degraded. Sorbents sequester chemicals in water through adsorption and absorption processes, enabling the elimination of these contaminants when the sorbents are removed from solutions. Traditionally, activated carbons have been commonly used as sorbents. However, their use can be expensive both from financial and energy standpoints, so attempts have been made to identify alternative sorbents.[3,6,12]

Natural biopolymers derived from low-cost, renewable biosources such as algae, plants, microbes, and animals represent promising foundations for sustainable alternatives.[6,13] In particular, polysaccharides and their derivatives
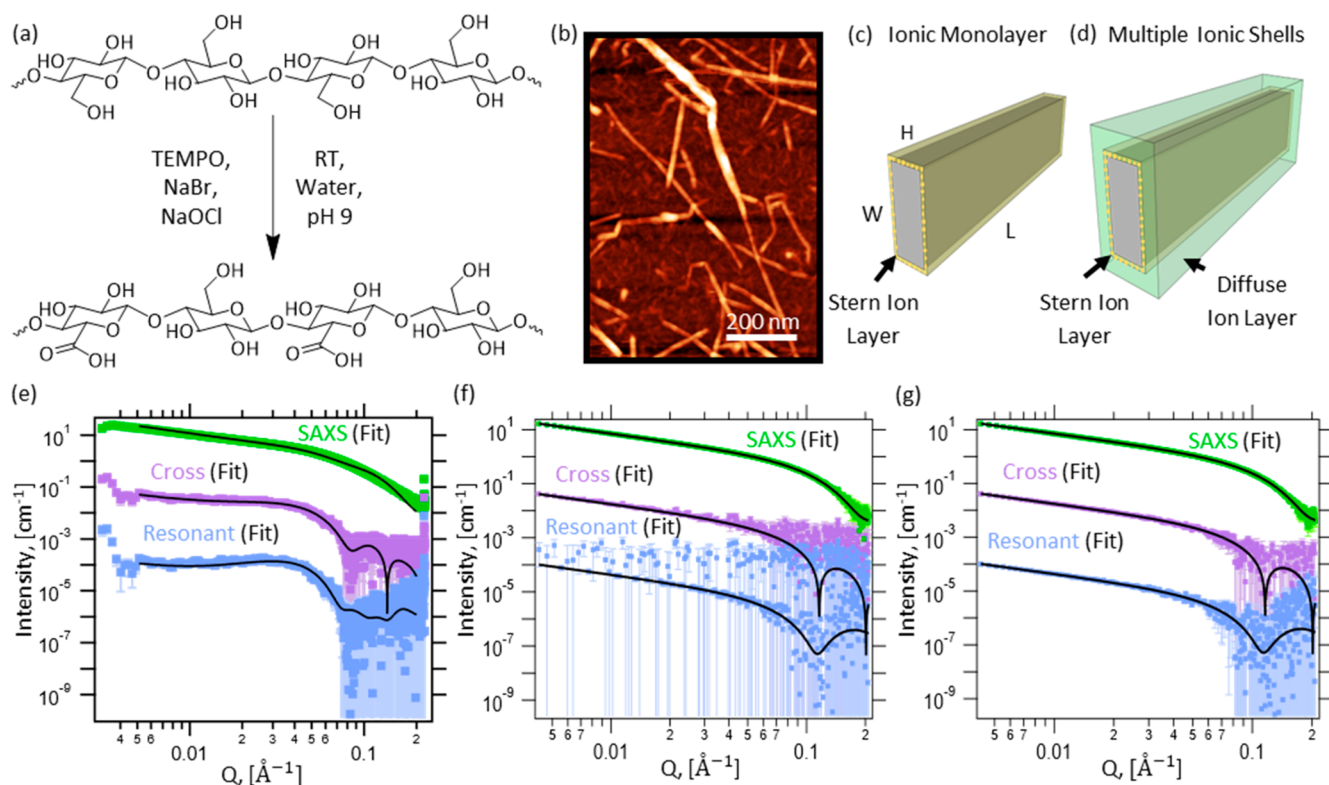
Figure 1. (a) Synthesis of carboxylic acid functionalized CNCs (*MxG*-CNC-COOH_X), where X is the surface density of carboxylic acid groups in mmol/kg. (b) AFM image of *MxG*-CNC-COOH_1100 on a mica substrate. (c) Representation of a Stern layer of ions (yellow) adsorbed in a monolayer to the CNC core (gray). (d) Representation of a diffuse layer of ions associated with the Stern layer and CNC core. (e) ASAXS data from *MxG*-CNC-COOH_1100 in 50 mM RbCl solution with parallelepiped model fits. Scattering components with error bars were obtained using the Sturhmann method with (f) inequality and (g) equality constraints fit to simulated X-ray scattering data from the parallelepiped model of CNCs as seen in Figure S7. The corresponding scattering components simulated from the model are shown as solid black lines.

have exhibited high removal efficiency for both inorganic contaminants such as heavy metals and organic pollutants such as dyes via adsorption. As such various polysaccharides, including chitosan[7,10,14] and cellulose,[15,16] have been utilized in water purification applications.[6] Cellulose is particularly promising as it is the most common biopolymer on the planet[17] and can act as an abundant, low-cost adsorbent with a surface that can be engineered through facile chemical modification to enhance the sorption capacity and selectivity.[18,19] Nanocellulose are nanosized particles of cellulose that can be obtained directly from the biosource.[13,18,20−22] Cellulose nanocrystals (CNCs) are a class of nanocellulose that consists of high aspect ratio nanoparticles that can be isolated from many different biosources, like cotton, wood, or grasses such as *Miscanthus* x *giganteus* (*MxG*).[13,23,24] Various charged moieties, such as carboxylates, sulfates, and phosphates, were introduced to the surface of CNCs. Studies have been conducted to evaluate the ability of these functionalized materials to remove inorganic contaminants such as Cr^{3+}, Pb^{2+}, and Cd^{2+} or charged organic dyes such as Methylene Blue and Crystal Violet.[18,25−39]

While these studies have shown that cellulose-based sorbents can effectively sequester various ionic contaminants, the spatial distribution of the resulting adsorbed species in and around the adsorbent has not been thoroughly investigated. The reason for this limited knowledgebase is that most characterization techniques do not reveal enough information about the differences in the arrangement of heavy metal ions

relative to that of the crystalline cellulose sorbent. Previous studies have employed adsorption isotherms combined with data fitting models (i.e., the Langmuir model) to determine the adsorption mechanism.[25] Other studies have utilized spectroscopic techniques like Fourier transform infrared (FTIR) spectroscopy and X-ray photoelectron spectroscopy (XPS) to investigate the mechanism behind metal ion adsorption.[26] These studies provide a very localized interfacial bonding structure and found the adsorption mechanism to be a combination of complexation between the ions and the surface functional groups as well as ion exchange.[26] However, these techniques lack information about the long-range diffuse three-dimensional distribution of the ions around the charged cellulose nanoparticles.

Anomalous small-angle X-ray scattering (ASAXS) has been used to characterize a variety of charged nanomaterials systems including polyelectrolyte brushes,[40,41] DNAs,[42−45] and polyoxometalates[46] to quantitatively determine the distribution of ions surrounding them. A typical ASAXS measurement records the changes in the small-angle X-ray scattering (SAXS) intensity from a sample of interest as a function of energy very near and traversing the absorption edge of an element of interest (resonant element) in the sample. The elemental sensitivity in the scattering pattern comes from the changes in the scattering contrast of the resonant elements near their absorption edges. After obtaining the energy-dependent scattering patterns, it is possible to extract the scattering contribution of the resonant element. In addition, the energy-

dependent scattering pattern can be directly analyzed via a physical model of the nanomaterial system.[47] The extraction method of scattering contributions from energy-dependent scattering patterns was first introduced by Stuhrmann[48−50] and is, hence, named the Stuhrmann method.[51] The extraction of the scattering components can be challenging on account of the weak scattering contribution from the resonant element and the presence of statistical fluctuations in the scattering patterns obtained experimentally. While this approach can be challenging, it does provide a direct way to examine the scattering contribution from the resonant elements. Alternatively, if the size and morphology of the nanomaterial being investigated are known, e.g., from real space imaging techniques such as electron microscopy or atomic force microscopy, then this information allows models of the distribution of ions surrounding the nanomaterial to be developed. Such models can then be used to either calculate the scattering contributions from the element of interest or calculate the energy-dependent scattering patterns.

Reported herein are studies of monovalent (Rb⁺), divalent (Sr²⁺), and trivalent (Y³⁺) ions adsorbed onto carboxylate functionalized cellulose nanocrystals (CNC-COOH) using ASAXS to determine the structure of the adsorbed ions and gain insight into the mechanism behind their adsorption. As one of the goals of this work is to show the feasibility of ASAXS to determine the ion distribution around CNCs and the role of electrostatic interactions, initial ASAXS experiments were carried out at the energies at which the absorption of the X-rays by the samples can be minimized while at the same time maintaining a strong X-ray scattering signal. In this regard, Rb⁺ with the K-edge X-ray absorption energy of 15.2 keV is a good initial choice of ion for these experiments. Sr²⁺ and Y³⁺ were selected as multivalent adsorption targets on account of their proximity to Rb⁺ in the periodic table enabling the effect of valency on ion adsorption to be investigated while comparing ions of similar size and with similar X-ray absorption edges of 16.105 and 17.038 keV for Sr and Y, respectively.

RESULTS AND DISCUSSION

Isolation and Functionalization of Cellulose Nanocrystals. CNCs were isolated from *Miscanthus* x *Giganteus* (*MxG*) before being oxidized to yield the *MxG*-CNC-COOH$_X$ following literature procedures.[13,52] In short, the *MxG* stalks undergo a series of steps, mechanical treatment, base washes, bleaching, and acid washes, in order to isolate the CNCs. (2,2,6,6-Tetramethylpiperidin-1-yl)oxyl (TEMPO)-mediated oxidation is then used to introduce carboxylic acid groups on the surface (Figure 1a). This oxidation method is commonly used in the literature to introduce negative charges on the surfaces of CNCs, which also enables electrostatically driven adsorption of cations to the carboxylate surface groups. The carboxylate density of the crystals was measured to be ca. X = 1100 mmol/kg via conductometric titration (Supporting Information Figure S1 and Table S1). In order to probe the effect of carboxylate density on ion adsorption, this TEMPO-mediated step was also carried out under different conditions with a lower ratio of TEMPO to NaOCl to synthesize a second batch of CNCs with a lower carboxylic acid density of ca. X = 740 mmol/kg. These two samples are termed *MxG*-CNC-COOH$_{1100}$ and *MxG*-CNC-COOH$_{740}$ to differentiate the higher and lower surface density samples. The successful functionalization was confirmed by FTIR showing the peak that corresponds to the formation of the carboxylate's carbonyl

stretch and TGA exhibiting the degradation and carbon/char yield associated with carboxylate functionalized CNCs (Figures S2 and S3, respectively). Crystallinity indexes of 0.78 and 0.71 were measured for the *MxG*-CNC-COOH$_{1100}$ and the *MxG*-CNC-COOH$_{740}$ samples, respectively (determined by WAXS, Figure S4). The *MxG*-CNC-COOH$_{1100}$ crystals were measured by AFM (Figure 1b) and found to have an average length of 250 ± 170 nm ($n = 700$) and average height and width of 2.4 $\pm$ 0.6 and 13 $\pm$ 2.0 nm ($n = 30$), respectively. The *MxG*-CNC-COOH$_{740}$ crystals were found to have dimensions of 300 $\pm$ 120 nm by 3.5 $\pm$ 0.7 nm by 8.5 $\pm$ 1.9 nm when measured with the same AFM procedure (Figure S5). However, the width measurement is artificially larger than the real width of the CNC crystals, on account of the tip broadening phenomenon (Figure S6). After accounting for this effect, the width of the CNCs is 3.5 $\pm$ 2.0 nm. These data are consistent with the literature values for *MxG*-CNCs.[13,24,52]

Parallelepiped Model of CNCs. The *MxG*-CNCs can be described as having a ribbon-like parallelepiped shape.[13] Thus, in order to extract metrical information from ASAXS data, multilayered parallelepiped models, as shown in Figure 1c,d, were used to describe the *MxG*-CNC-COOH$_X$ nanoparticles and the distribution of ions surrounding them in an aqueous environment. As per the model, the bare CNC is the core and the initial shell surrounding the core represents the Stern layer of adsorbed metal ions on the nanocrystal surfaces. The thickness of the Stern layer is defined as the ionic diameter of the appropriate metal ion.[53−55] A subsequent layer on top of the Stern layer is included in the model as a diffuse layer of ions surrounding the nanoparticle. Additional details about the model are discussed in the Supporting Information, Section S1.

Simulation. To validate the parallelepiped model, the model was applied with the XModFit program[56] to the simulated energy-dependent X-ray scattering data (Figure S7) based on CNCs of with dimensions obtained from the AFM measurements ($H = 2.4$ nm, $W = 3.5$ nm, $L = 250.0$ nm), with metal ions surrounding them in an aqueous environment. The dimensions used for the simulations are the values obtained from the AFM measurements of MxG-CNC-COOH$_{1100}$. The metal ions used for the simulation were Rb⁺ ions with a uniform density of 0.3 g/cm³ adsorbed onto the CNC surfaces and 0.00855 g/cm³ (100 mM) in the bulk aqueous phase. The thickness of the Stern layer is considered the ionic diameter of Rb⁺ (0.332 nm). The energies chosen to simulate the intensities are within 1 keV of the Rb K-Edge (i.e., 14.2− 15.2 keV). In order to be able to simulate the energy-dependent SAXS data that resemble experimental data (shown in Figure 1e) were added to the simulated intensities. As the energy dependence is relatively weak, a point at $Q = 0.021$ Å^{-1} is taken from each simulated spectrum and plotted against energy (Figure S7) and the data clearly show the expected increase in intensity as scattering factor (f') increases with incident X-ray energy moving away from the absorption edge of the metal ion.

The Stuhrmann method is applied to the energy-dependent simulated intensities to obtain different scattering components with both the inequality and equality constraints (Supporting Information Section S2). On account of the presence of statistical variance in the data, variances in the scattering components were also observed. It is important to note that the inequality constraint only provides a lower limit for the resonant term and is therefore not capable of providing a well-

constrained estimate of weak "resonant scattering" from metals ions, as evident from the large uncertainties shown in Figure 1f at low Q values in the absence of statistical variances. The equality constraint, on the other hand, provides constrained estimates of the resonant term for the ion distribution of the parallelepiped model, as shown in Figure 1g. While the equality constraint can provide a constrained estimate, it is to be used with caution as the minima of energy-dependent SAXS data might provide artifacts and should be verified with simulations similar to those presented here. Satisfied that the equality constraint does not produce artifacts and provides a better fit for the parallelepiped model when applied to the simulated data, the same equality constraint was applied to the experimental energy-dependent SAXS data to obtain the scattering components and subsequently the metrical information about the CNCs and the distribution of ions surrounding them.

The parallelepiped model was initially used to fit the scattering components obtained from the ASAXS data and in the process to determine the distribution of the adsorbed Rb^+ ions in the Stern layer around MxG-CNC-COOH$_X$. The model was also used to refine the dimensions of the MxG-CNC-COOH$_X$ nanoparticles in the samples starting with the anticipated dimensions from AFM data. The length of 250 nm was input as a constant to reduce the number of variables in the fitting. The heights of the crystals determined by AFM and ASAXS match within error. As mentioned previously, the width of the crystals will be overestimated in the AFM measurement on account of the tip-broadening phenomenon. However, taking the size of the AFM tip into account (Figure S6), the width calculated by the model agrees with the AFM measurements, within error. By comparing the size of the crystals as determined by the model ($H = 2.8 \pm 0.12$ nm, $W = 4.2 \pm 0.18$ nm, $L = 250$ nm) with the size of crystals as determined by AFM ($H = 2.4 \pm 0.6$ nm, $W = 3.5 \pm 2.0$ nm, $L = 250 \pm 170$ nm), the model can be validated as it generates accurate metrical data from the anomalous scattering components as shown in Figure 1e.

Investigation of the Adsorption of the Rb^+ Ions on the CNCs. With the validation of the parallelepiped model in hand, the next step was to explore the metal ion adsorption on the CNCs. To this end the MxG-CNC-COOH$_{740}$ and MxG-CNC-COOH$_{1100}$ samples were soaked in 50 mM RbCl solutions, which were then studied using ASAXS. Interestingly, the one-dimensional ASAXS data (Figure 2) shows a shift in the form factor for these two samples. This shift is most clearly seen in the resonant and cross terms, as the terms for MxG-CNC-COOH$_{1100}$ exhibit higher intensities than the corresponding MxG-CNC-COOH$_{740}$ terms. Since the resonant term is correlated with Rb^+ for these experiments, the increase in the intensity of the resonant term is indicative of a larger amount of Rb^+ around the CNC in those samples. In order to extract metrical information about the adsorbed ions, several parameters such as the density of Rb^+ within each layer around the CNCs were varied in the parallelepiped model to generate the best fit. By fitting the parallelepiped model to the data, it was determined that a peak concentration of Rb^+ ions, which is orders of magnitude larger than the bulk concentration, forms within 3.32 Å of the MxG-CNC-COOH$_{740}$ surface and quickly returns to the bulk concentration beyond this distance. This result is indicative of the formation of a Stern layer, which has a thickness on the order of the ionic diameter of the adsorbed ion around the nanoparticle (Figure 1c). Although the MxG-

Figure 2. ASAXS data of MxG-CNC-COOH$_{740}$ and MxG-CNC-COOH$_{1100}$ soaked in 200 mM RbCl split into their respective SAXS, cross, and resonant terms with the parallelepiped model fits for each set of data shown in gray.

CNC-COOH$_{1100}$/RbCl samples also exhibited a peak concentration of Rb^+ ions within the same distance from the crystal surface, a single Rb^+ layer in the parallelepiped model was insufficient to fit the ASAXS data. Thus, the model was adjusted to include multiple Rb^+ shells around the CNC core (Figure 1d). This multilayer model fits the MxG-CNC-COOH$_{1100}$/RbCl data by adding a diffuse layer on top of the highly concentrated Stern layer. A diffuse layer around a Stern layer is a known phenomenon that is observed in charged colloids in accordance with the Gouy−Chapman and Grahame models for electrolyte adsorption.[55] The introduction of a diffuse layer for the MxG-CNC-COOH$_{1100}$/RbCl samples implies that the Rb^+ could not fill in the Stern layer in a manner that could balance the surface potential of the charged CNCs. Since the Stern layer is composed of Rb^+ ions adsorbing to the surface as well as water molecules solvating both the ions and the surface, these solvent molecules limit the maximum capacity of the Stern layer. The combination of electrostatic interactions and hydrostatic repulsion leads to the formation of the diffuse layer.[55] In the case of the MxG-CNC-COOH$_{740}$/RbCl samples, the Rb^+ ions can occupy the Stern layer such that the surface potential is sufficiently neutralized without the formation of a diffuse layer.
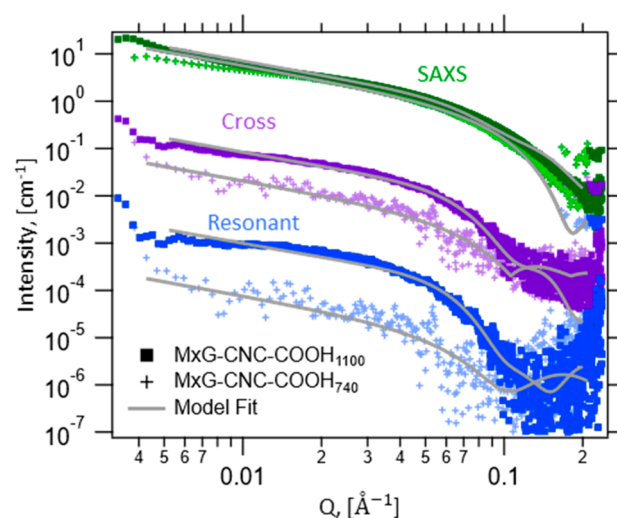
After fitting the ASAXS data generated by the MxG-CNC-COOH$_{1100}$ and MxG-CNC-COOH$_{740}$/Rb^+ samples with the parallelepiped model (Figures S8 and S11), the adsorbed Rb^+ ion density was extracted from the model and compared to the surface charge density for each sample as determined by the conductometric titration (Figure S1). The MxG-CNC-COOH$_{1100}$ shows a maximum total Rb^+ ion adsorption in both the Stern and diffuse layers of 14700 ± 265 mmol of Rb^+/(kg of CNC) with a maximum Rb^+ ion density in the Stern layer of 4350 ± 54 mmol of Rb^+/(kg of CNC). MxG-CNC−COOH$_{740}$ exhibits a maximum Rb^+ ion adsorption of 1680 ± 51 mmol of Rb^+/(kg of CNC) in the monolayer surrounding the CNC. Comparison of the Rb^+ ion density adsorbed on to MxG-CNC-COOH$_{1100}$ and MxG-CNC-COOH$_{740}$ (Figure 3) shows that the multilayer adsorption (Stern layer plus the surrounding diffuse layer) of the MxG-CNC-COOH$_{1100}$ results in significantly more ions surrounding
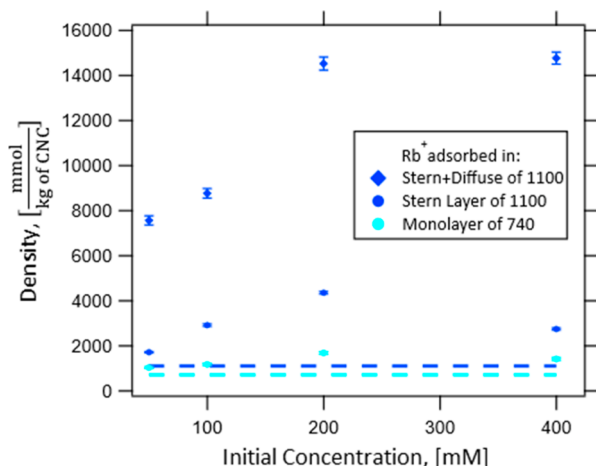
Figure 3. Comparison of the density of Rb^+ ions adsorbed on the *MxG*-CNC-$COOH_{740}$ to the density of Rb^+ ions on the *MxG*-CNC-$COOH_{1100}$ for various concentrations (50, 100, 200, and 400 mM RbCl) and to the surface density of carboxylates on both the *MxG*-CNC-$COOH_{740}$ and the *MxG*-CNC-$COOH_{1100}$ as represented by the horizontal dashed lines. The error bars on the density values were obtained from fitting the ASAXS data with rectangular parallelepiped model with 68% confidence interval.

these CNCs. In both the *MxG*-CNC-COOH samples the number of adsorbed cations is greater than the amount of negative charge on their surfaces (horizontal dashed lines in Figure 3). This significant ion adsorption implies that the driving force behind this effect is more than the ionic electrostatic interactions between the metal ions and carboxylates on the surface. Additional specific adsorption sites for the Rb^+ could be provided by the diols present along the cellulose chains—the hydroxyl groups on the C2 and C3 carbons of the cellulose repeat unit can associate with the Rb^+ through ion—dipole interactions. The number of diols on the surface of the CNCs is approximately equal to the number of carboxylate groups on the surface, and as such the presence of the diols effectively doubles the number of potential adsorption sites along the hydrophilic faces of the CNC surface to 2200 mmol/(kg of CNC) on the *MxG*-CNC-$COOH_{1100}$ samples. However, these potential adsorption sites are still less than the calculated amount of Rb^+ ions adsorbed to the CNCs. Therefore, additional Rb^+ ion adsorption sites are needed to account for the additional Rb^+ in the Stern layer. Adsorption to these other sites may be driven by a chaotropic effect. It has been shown that poorly solvated monovalent ions (chaotropic ions) like Rb^+ are capable of adsorbing onto oppositely charged hydrophobic particles through interactions between the ions and hydrophobic regions of the particles.[57] The poor solvation environment around the hydrophobic surface interacts favorably with the poorly solvated chaotropic ion, leading to adsorption and entropic gain by releasing the solvent molecules around both the ion and the hydrophobic surface. As recent studies utilizing three-dimensional AFM corroborated by molecular dynamic simulations have shown, certain cellulose crystal faces like the (200) crystal face exhibit regions void of cellulose—water hydrogen bonds, indicating that these faces are hydrophobic.[58] Furthermore, CNCs have been shown to exhibit amphiphilicity since these nanoparticles can stabilize oil—water interfaces by acting as nanosized surfactants.[59−62] As such, the CNCs have hydrophobic regions which can provide additional adsorption sites for chaotropic

ions. The combination of both electrostatic and chaotropic adsorption sites for the Rb^+ ions enables a higher than expected concentration of Rb^+ to reside in the Stern layer.

The structure and adsorption process also depend on the concentration of the metal ions in the initial solution. By varying the feed solution's concentration between 50, 100, 200, and 400 mM, it was observed that the adsorbed Rb^+ in the Stern layer peaks at 1680 ± 51 mmol of Rb^+/(kg of CNC) around an initial solution concentration of 200 mM RbCl for the *MxG*-CNC-$COOH_{740}$ samples (Figure 3). For the *MxG*-CNC-$COOH_{1100}$ samples, the total amount of adsorbed Rb^+ appears to reach a plateau from 200 to 400 mM RbCl with total adsorbed ion densities of 14500 ± 290 and 14700 ± 265 mmol of Rb^+/(kg of CNC), respectively (Figure 3). However, as the concentration of the initial solution increases, the Rb^+ ions appear to be less strongly associated with the *MxG*-CNC-$COOH_{1100}$ surface since the density of ions in the Stern layer decreases from 4350 ± 54 to 2740 ± 43 mmol of Rb^+/(kg of CNC) after 200 mM. This decline in density of ions in the Stern layer implies that at higher concentrations solute—solute and solute—solvent interactions begin to become more favorable than some of the solute—substrate interactions, which corresponds with the shortening of the Debye length as salt concentration increases.

Effect of Multivalent Ions. After investigating the adsorption of Rb^+ ions to the CNC surface, the adsorption of two multivalent ions, namely, Sr^{2+} and Y^{3+}, to the CNCs was explored. Similar to the *MxG*-CNC-$COOH_{740}$/RbCl samples, a monolayer parallelepiped model as illustrated in Figure 1b fits the ASAXS data sufficiently well (see Figures S12 and S13). These data indicate that the low surface charge density of *MxG*-CNC-$COOH_{740}$ only supports the formation of an adsorbed Stern layer of these ions. As shown in Figure 4a, for the *MxG*-CNC-$COOH_{740}$ samples, the adsorption isotherms exhibit a maximum in the adsorbed ion density of 1200 ± 51 mmol of Sr^{2+}/(kg of CNC) and 888 ± 26 mmol of Y^{3+}/(kg of CNC) for Sr^{2+} and Y^{3+}, respectively. Similarly, type *mx* adsorption isotherms with a maximum have been seen in other cellulose-based substrates when ion pairs are being adsorbed to the surface after initial cation exchange.[63−66] This maximum in the shape of the adsorption curve implies that as the bulk concentration increases the solute—solute interactions within the solution start to overcome the solute—substrate interactions.[63] It is likely that as the concentration of salt in the solution increases, the driving force leading to the adsorption of ions and ion pairs decreases with the shortening of the Debye length and an electrical screening of the surface.[65,66] The maximum adsorbed ion density occurs at different initial ion concentrations for the *MxG*-CNC-$COOH_{740}$ samples, 200, 200, and 50 mM for Rb^+, Sr^{2+}, and Y^{3+}, respectively (Figure 4a). Unlike Rb^+, Sr^{2+} and Y^{3+} ions are not chaotropic but kosmotropic such that the hydration sheaths around the Sr^{2+} and Y^{3+} ions are more stable, and as a result the chaotropic interaction with the hydrophobic regions of the CNCs is less favorable with such ions. Thus, the primary driving forces for Sr^{2+} and Y^{3+} adsorption appear to be electrostatic in nature with a combination of specific chemical interaction between the Sr^{2+} or Y^{3+} and the carboxylate and diol moieties on the surface as well as ion—ion correlations between the metal ions and counterions. As observed in Figure 4a, Sr^{2+} exhibits a maximum adsorbed ion density at 200 mM initial concentration, whereas Y^{3+} appears to saturate at 50 mM before decreasing as the initial concentration of the solution is
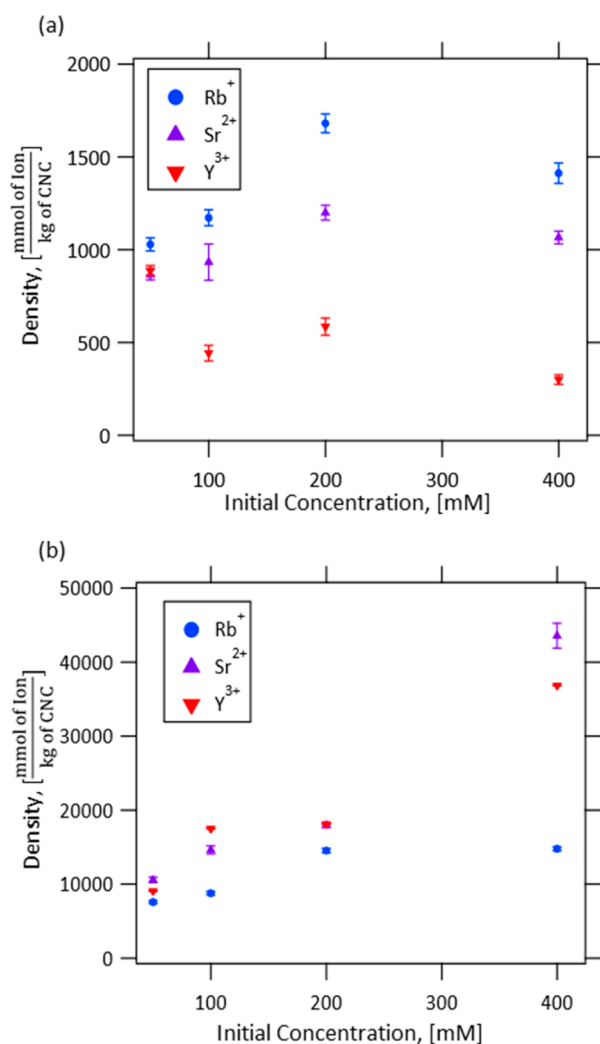
Figure 4. (a) Density of Rb^+, Sr^{2+}, and Y^{3+} adsorbed into the Stern layer around *MxG*-CNC-COOH$_{740}$ as the initial concentration of these ions increases (50, 100, 200, and 400 mM). (b) Total adsorbed ion density of Rb^+, Sr^{2+}, and Y^{3+} in both the Stern and diffuse layers normalized by the mass of *MxG*-CNC-COOH$_{1100}$ in each sample as the initial ion concentration increases (50, 100, 200, and 400 mM). The error bars on the density values were obtained from fitting the ASAXS data with the rectangular parallelepiped model with a 68% confidence interval.

increased. The shift in maximum adsorption density from 200 mM in the case of Sr^{2+} to 50 mM in the case of Y^{3+} is expected for the electrostatic adsorption of kosmotropic ions like Sr^{2+} and Y^{3+}. Since the Debye length scales with the ion valency, the increased salt concentration of the bulk solution will have a greater electrostatic effect on the more highly charged ions. Since the Y^{3+} ion is trivalent compared to the divalent Sr^{2+} ion, the surface will likely be more effectively screened at lower concentrations of Y^{3+} than at equal concentrations of Sr^{2+}. The differences in the electrostatic screening of the surface may contribute to the Stern layer saturating at lower concentrations for Y^{3+} because the primary driving force is electrostatic in nature.

When the surface charge density on the CNCs is increased, the *MxG*-CNC-COOH$_{1100}$ samples adsorb more multivalent ions than the *MxG*-CNC-COOH$_{740}$ samples. As with the RbCl absorption data, a monolayer parallelepiped model is insufficient to fit these data. Therefore, a multilayer

parallelepiped model illustrated in Figure 1d is used to fit the Sr^{2+} and Y^{3+} adsorption data for the *MxG*-CNC-COOH$_{1100}$ samples. The formation of both a Stern and diffuse layer of adsorbed ions is expected for kosmotropic ions such as Sr^{2+} and Y^{3+}. As Figure 4b shows, the adsorbed ion densities of Sr^{2+} and Y^{3+} continue to increase as the initial concentrations increase, showing that adsorption becomes easier as more ions are present and adsorb. This continued increase in adsorbed ions is seen in other kosmotropic ion adsorption isotherms as ion−ion correlations encourage more ions to fill the diffuse layer and potentially form additional layers as previous layers saturate.[63] Unlike the multivalent ions, the Rb^+ isotherm plateaus at higher concentrations, indicative of saturation instead of the growth of additional adsorbed layers. This phenomenon could be caused by the limited amount of hydrophobic surface area on the sample such that once these regions are covered by Rb^+ ions, the chaotropic driving force substantially weakens and the Stern and diffuse layers saturate. The nature of the adsorption at these higher concentrations further supports the notion that the Sr^{2+} and Y^{3+} ions adsorbed through electrostatic driving forces while the Rb^+ ions are adsorbed at least partially by different mechanisms.

CONCLUSIONS

A parallelepiped model was developed to analyze ASAXS data from parallelepiped-shaped nanoparticles like CNCs. This model was used in combination with ASAXS studies to give insights into the nature of metal ion binding to CNCs. In particular, it was shown that the structure of ions adsorbed to *MxG*-CNC-COOH$_X$ nanoparticles shifts as the carboxylate surface density, X, is increased. In addition, the data show that *MxG*-CNC-COOH$_X$ can leverage chaotropic, electrostatic, and complexation mechanisms to adsorb ions to their surfaces. The knowledge of these structures and mechanisms can help inform the design of improved cellulose-based sorbents for water purification applications. For example, understanding the dependence of the adsorbed ion distribution on initial concentration could improve efforts to optimize contaminant removal informing what contaminated sources could be ideal for purification with cellulose-based sorbents. This adsorbed molecular structure will likely vary between different contaminants. As such, future studies into the structure of other relevant water contaminants such as Hg, Cd, Pb, Cr, or As on cellulose nanocrystals may be of interest. Additional methods of improving the adsorptive capacity of these sorbents like polymer grafting may also be studied.

MATERIALS AND METHODS

Materials. *Miscanthus x Giganteus* (*MxG*) pulp was provided by Aloterra Energy, LLC. Sodium hydroxide (NaOH), sodium hypochlorite (NaOCl), and acetic acid were purchased from Thermo Fisher Scientific. Sodium chlorite (NaClO$_2$), hydrochloric acid (HCl), 2,2,6,6-tetramethylpiperidine 1-oxyl (TEMPO), and sodium bromide (NaBr) were purchased from Millipore Sigma. Rubidium chloride (RbCl), strontium chloride (SrCl$_2$), and yttrium chloride (YCl$_3$) were purchased from Sigma-Aldrich. All water used was deionized in-house, and all chemicals were used as-received without further purification.

Cellulose Nanocrystal Isolation from *Miscanthus x Giganteus*. Ground *MxG* stalks (266.6 g) were soaked in 4 L of 2 wt % sodium hydroxide solution at room temperature for 24 h. The stalks were then treated twice more with 4 L of 2 wt % sodium hydroxide solutions at 95 °C for 24 h each. After each treatment, the stalks were washed with deionized (DI) water until the permeate was neutral pH.

The pulp was then suspended in 4 L of 2 wt % sodium chlorite solution and 15 mL of glacial acetic acid and heated to 70 °C for 2 h. After the reaction, the solution was vacuum filtered and washed with DI water until the solid was white with no other color. For these samples, the color of the *MxG* pulp remained white. To isolate CNCs, hydrolysis was carried out by suspending the bleached white pulp in 4 L of 1 M HCl. This slurry was then heated to 75 °C and stirred for 15 h. The mixture was then cooled to room temperature before being vacuum filtered and rinsed with DI water until the permeate was neutral. The solids were then subjected to dialysis with DI water for 5 days, with the external solution being replaced twice every day. The solutions were then freeze-dried to obtain the alcohol functionalized *MxG* CNCs (*MxG*-CNC-OH) as a white crystalline solid.

Synthesis of *MxG*-CNC-COOH$_X$ from *MxG*-CNC-OH via TEMPO Oxidation. In order to synthesize the *MxG*-CNC-COOH$_{1100}$ samples, TEMPO oxidation was conducted immediately after isolating the MxG-CNC−OH, without drying, following the previously published procedure with slight modifications.[13,52] The *MxG*-CNC−OH isolated from 250 g of dried *MxG* stalks were suspended in solution with 7.5 g of TEMPO, and 75 g of NaBr. A 110 mL aliquot of NaOCl was then added to this solution after which the pH was adjusted to 10.5 with 10 M NaOH. The pH was maintained between 10 and 11 for 3 h at which time the resulting *MxG*-CNC-COOH$_{1100}$ was centrifuged at 10000 rpm and resuspended approximately 5 times in DI water to purify the sample. The nanoparticles were suspended in DI again before being freeze-dried to yield a fluffy white powder of *MxG*-CNC-COOH$_{1100}$.

In order to synthesize the *MxG*-CNC-COOH$_{740}$ samples, 21.6 g of *MxG*-CNC-OH was dispersed into 1500 mL of DI water. Simultaneously, 1.687 g of TEMPO, 16.926 g of NaBr, and 138.109 g of NaOCl were dissolved in 500 mL of DI water. These two solutions were then mixed together, and the pH was adjusted to 10 with NaOH and HCl. Once at pH 10, the reaction was allowed to proceed for 4.5 h with the pH being checked every half-hour. The reaction was then quenched with 40 g of sodium chloride before being filtered and washed with DI water. The solid was redispersed in DI water and dialyzed for 5 days before being freeze-dried to produce *MxG*-CNC-COOH$_{740}$.

Conductometric Titration. The functional group density of the *MxG*-CNC-COOH$_X$ samples was determined by conductometric titration. A 75 mg amount of *MxG*-CNC-COOH$_X$ was dispersed into 150 mL of DI water using sonication. A 15 μL aliquot of 12 M hydrochloric acid was added to 50 mL of the CNC dispersion to lower the solution's pH to 2−3. This suspension was then titrated with 0.01 M sodium hydroxide. In order to determine the charge density on the surface of the CNCs, the volume of 0.01 M sodium hydroxide used to titrate the weak acid functional groups in the conductometric titration was determined as shown in Figure S1. The length of the initial trend line represents the volume of 0.01 M NaOH used to titrate the strong acid functional groups, while the plateau region corresponds to the weak acid functional groups. From the volume of NaOH used to titrate these functional groups, the functional group density on the CNC surface can be determined by

$$\text{functional group density} = \frac{CV_{\text{NaOH}}}{M}$$

where C is the concentration of NaOH, V_{NaOH} is the volume of NaOH used to titrate the functional groups based on the difference between where the trendlines intersect, and M is the mass of CNCs in kg.

Thermogravimetric Analysis. The thermal stability of each CNC sample was measured through thermogravimetric analysis. For each sample, approximately 5 mg of CNCs was heated from ambient temperature to 600 °C at a rate of 20 °C/min under a nitrogen atmosphere at a flow rate of 25 mL/min.

Degree of Crystallinity. Wide-angle X-ray scattering (WAXS) conducted at the 12-ID-B beamline at the Advanced Photon Source at Argonne National Laboratory was used to determine the degree of crystallinity of the CNCs after hydrolysis and oxidation. The CNCs were packed tightly into a washer and held in place between two

pieces of Kapton tape. The data were then processed using the SAXS GUI software at the beamline before being analyzed with the SAS Irena package in IGOR Pro 7.[69] The crystallinity index of the samples was determined by the peak deconvolution method with a Gaussian fit.

Atomic Force Microscopy. Atomic force microscopy (AFM) was conducted on a Cipher ES Environmental AFM. Samples were prepared on a freshly cleaved mica surface by first drop-casting poly(L-lysine), gently rinsing with DI water, and then drop-casting the desired CNC sample suspended in DI water at 0.005 wt %. The solution was allowed to sit for 3 min before once again gently rinsing with DI water before drying overnight. The samples were imaged in tapping mode with FS-1500 probes from Asylum Research and data was analyzed with Gwyddion software (Czech Metrology Institute).

Anomalous Small-Angle X-ray Scattering (ASAXS). The *MxG*-CNC-COOH$_X$ were vacuum-cast onto PVDF membranes to form CNC nanopapers. PVDF was selected as the support membrane so that the nanopapers could be delaminated from the surface to create freestanding *MxG*-CNC-COOH$_X$ films. In order to access the information about the distribution of cations, namely, Rb$^+$, Sr^{2+}, and Y^{3+}, energy-dependent small-angle X-ray scattering (SAXS) or ASAXS measurements were performed on the chloride salt solution soaked *MxG*-CNC-COOH$_X$ samples. The ASAXS measurements were performed with X-rays of 20 energies within 1 keV below the K-absorption edges of Rb (15.2 keV), Sr (16.105 keV), and Y (17.038 keV), respectively. The measurements were performed at the ASWAXS facility of the NSF's ChemMatCARS, Sector-15 of Advanced Photon Source. The energy values were chosen in a way that the real part of the scattering factor (f') of Rb, Sr, and Y could be equally spaced. For better understanding of the interaction of the cations with the *MxG*-CNC-COOH$_X$ surfaces, the ASAXS measurements were performed with increasing concentrations (50, 100, 200, and 400 mM) of the chloride salts of the cations. The samples in the form of thin films were loaded in quartz capillary tubes of 1.5 mm outer diameter with 0.010 mm wall thickness. Different samples were prepared by pouring salt solutions of different concentrations into the capillary tube to soak the films completely. ASAXS measurements were collected from the regions of the capillary tubes where the soaked films were present and from the regions with only solutions which were considered as backgrounds. The salt solution scattering acts as a better background because it also takes care of the fluorescence background coming from the solution when the X-ray energies are closer to the absorption edges. It is important that the changes in the intensity due to X-ray beam energy only come from the changes in the scattering from the resonant element and not from the beam induced changes in the samples. Due to this reason, samples were tested for X-ray beam induced changes with varying lengths of exposure to the X-ray beam. These experiments established the maximum time of exposure for the ASAXS experiments to ensure that the samples were not damaged during the process. Apart from the samples and backgrounds, ASAXS data were also measured for an empty capillary tube, air, and glassy carbon for absolute scale normalization. Background subtraction and absolute scale normalization were done on the azimuthally averaged ASAXS data using software "XAnoS" developed at NSF's ChemMatCARS.[67] Energy dependent azimuthally averaged data after background subtraction and absolute scale normalization were further processed to obtain SAXS term (I_S), cross-term (I_C), and Resonant-term (I_R) as per the Stuhrmann method, discussed in detail in Supporting Information eqs S2−S8.

Parallelepiped Model Development. Two different functions, "Parallelepiped_Uniform" and "Parallelepiped_Uniform_Edep", were created in the ASAXS category of the XModFit Software developed by ChemMatCARS[68] and available freely from Github[56] to simulate ASAXS scattering intensity from multilayered-parallelepiped structures. Parallelepiped_Uniform calculates different scattering components ("SAXS-term", "Cross-term", "Resonant-term", and "Total") from the above-mentioned multilayered-parallelepiped model, whereas Parallelepiped_Uniform_Edep calculates energy-dependent total X-ray scattering from the multilayered-parallelepiped model. More

details about the functions are available in Supporting Information, Section S1. This model can fit the data by varying several parameters. For these samples, the width and height of the inner core were varied while the length was held constant at the average length of the CNCs as determined by the AFM measurements. Additionally, the concentration of adsorbed ions in the Stern were varied while the size of the Stern layer was held constant at the ionic diameter of the metal ion being measured by the ASAXS experiment. Additional layers beyond the Stern layer were also included with varying ion densities and lengths for each layer if they improved the model's ability to fit the data as they did for the case of the *MxG*-CNC-COOH$_{1100}$ samples.

ASSOCIATED CONTENT

ⓈⒾ Supporting Information

The Supporting Information is available free of charge at https://pubs.acs.org/doi/10.1021/acsnano.3c06140.

AUTHOR INFORMATION

Corresponding Authors

Stuart J. Rowan — *Pritzker School of Molecular Engineering and Department of Chemistry, University of Chicago, Chicago, Illinois 60637, United States; Chemical Science and Engineering Division and Center for Molecular Engineering, Argonne National Laboratory, Lemont, Illinois 60434, United States;* ⓘ orcid.org/0000-0001-8176-0594; Email: stuartrowan@uchicago.edu

Matthew V. Tirrell — *Pritzker School of Molecular Engineering, University of Chicago, Chicago, Illinois 60637, United States; Materials Science Division and Center for Molecular Engineering, Argonne National Laboratory, Lemont, Illinois 60434, United States;* ⓘ orcid.org/0000-0001-6185-119X; Email: mtirrell@uchicago.edu

Authors

Harrison R. Paul — *Pritzker School of Molecular Engineering, University of Chicago, Chicago, Illinois 60637, United States;* ⓘ orcid.org/0000-0001-6806-1908

Mrinal K. Bera — *NSF's ChemMatCARS, Pritzker School of Molecular Engineering, University of Chicago, Chicago, Illinois 60637, United States;* ⓘ orcid.org/0000-0003-0698-5253

Nicholas Macke — *Pritzker School of Molecular Engineering, University of Chicago, Chicago, Illinois 60637, United States;* ⓘ orcid.org/0000-0001-5072-7441

Complete contact information is available at:
https://pubs.acs.org/10.1021/acsnano.3c06140

Notes

The authors declare no competing financial interest.

ACKNOWLEDGMENTS

REFERENCES

(1) Vörösmarty, C. J.; Green, P.; Salisbury, J.; Lammers, R. B. Global Water Resources: Vulnerability from Climate Change and Population Growth. *Science* **2000**, *289* (5477), 284−288.

(2) Vörösmarty, C. J.; McIntyre, P. B.; Gessner, M. O.; Dudgeon, D.; Prusevich, A.; Green, P.; Glidden, S.; Bunn, S. E.; Sullivan, C. A.; Liermann, C. R.; Davies, P. M. Global Threats to Human Water Security and River Biodiversity. *Nature* **2010**, *467* (7315), 555−561.

(3) Crini, G. Non-Conventional Low-Cost Adsorbents for Dye Removal: A Review. *Bioresour. Technol.* **2006**, *97* (9), 1061−1085.

(4) Sahithya, K.; Das, D.; Das, N. Effective Removal of Dichlorvos from Aqueous Solution Using Biopolymer Modified MMT−CuO Composites: Equilibrium, Kinetic and Thermodynamic Studies. *J. Mol. Liq.* **2015**, *211*, 821−830.

(5) Keith, L. H.; Telliard, W. A. Priority Pollutants. I. A Perspective View. *Environ. Sci. Technol.* **1979**, *13* (4), 416−423.

(6) Nasrollahzadeh, M.; Sajjadi, M.; Iravani, S.; Varma, R. S. Starch, Cellulose, Pectin, Gum, Alginate, Chitin and Chitosan Derived (Nano)Materials for Sustainable Water Treatment: A Review. *Carbohydr. Polym.* **2021**, *251*, No. 116986.

(7) Khan, S. B.; Ali, F.; Kamal, T.; Anwar, Y.; Asiri, A. M.; Seo, J. CuO Embedded Chitosan Spheres as Antibacterial Adsorbent for Dyes. *Int. J. Biol. Macromol.* **2016**, *88*, 113−119.

(8) Albukhari, S. M.; Ismail, M.; Akhtar, K.; Danish, E. Y. Catalytic Reduction of Nitrophenols and Dyes Using Silver Nanoparticles @ Cellulose Polymer Paper for the Resolution of Waste Water Treatment Challenges. *Colloids Surf. A Physicochem Eng. Asp* **2019**, *577*, 548−561.

(9) Sun, Y.; Zhou, G.; Xiong, X.; Guan, X.; Li, L.; Bao, H. Enhanced Arsenite Removal from Water by Ti(SO4)2 Coagulation. *Water Res.* **2013**, *47* (13), 4340−4348.

(10) Elwakeel, K. Z.; Guibal, E. Arsenic(V) Sorption Using Chitosan/Cu(OH)2 and Chitosan/CuO Composite Sorbents. *Carbohydr. Polym.* **2015**, *134*, 190−204.

(11) *2012 Guidelines for Water Reuse*, EPA/600R-12/618; U.S. Environmental Protection Agency (EPA), 2004.

(12) Crini, G.; Lichtfouse, E.; Wilson, L. D.; Morin-Crini, N. Conventional and Non-Conventional Adsorbents for Wastewater Treatment. *Environ. Chem. Lett.* **2019**, *17* (1), 195−213.

(13) Cudjoe, E.; Hunsen, M.; Xue, Z.; Way, A. E.; Barrios, E.; Olson, R. A.; Hore, M. J. A.; Rowan, S. J. Miscanthus Giganteus: A Commercially Viable Sustainable Source of Cellulose Nanocrystals. *Carbohydr. Polym.* **2017**, *155*, 230−241.

(14) Mende, M.; Schwarz, D.; Steinbach, C.; Boldt, R.; Schwarz, S. The Influence of Salt Anions on Heavy Metal Ion Adsorption on the Example of Nickel. *Materials* **2018**, *11* (3), 373.

(15) Mautner, A.; Lee, K. Y.; Tammelin, T.; Mathew, A. P.; Nedoma, A. J.; Li, K.; Bismarck, A. Cellulose Nanopapers as Tight

Aqueous Ultra-Filtration Membranes. *React. Funct Polym.* **2015**, *86*, 209−214.

(16) Mautner, A.; Maples, H. A.; Sehaqui, H.; Zimmermann, T.; Perez de Larraya, U.; Mathew, A. P.; Lai, C. Y.; Li, K.; Bismarck, A. Nitrate Removal from Water Using a Nanopaper Ion-Exchanger. *Environ. Sci.: Water Res. Technol.* **2016**, *2* (1), 117−124.

(17) Habibi, Y.; Lucia, L. A.; Rojas, O. J. Cellulose Nanocrystals: Chemistry, Self-Assembly, and Applications. *Chem. Rev.* **2010**, *110* (6), 3479−3500.

(18) Voisin, H.; Bergström, L.; Liu, P.; Mathew, A. P. Nanocellulose-Based Materials for Water Purification. *Nanomaterials (Basel)* **2017**, *7* (3), 57.

(19) Yu, X.; Tong, S.; Ge, M.; Wu, L.; Zuo, J.; Cao, C.; Song, W. Adsorption of Heavy Metal Ions from Aqueous Solution by Carboxylated Cellulose Nanocrystals. *Journal of Environmental Sciences* **2013**, *25* (5), 933−943.

(20) Dufresne, A. Nanocellulose: A New Ageless Bionanomaterial. *Mater. Today* **2013**, *16* (6), 220−227.

(21) Capron, I.; Rojas, O. J.; Bordes, R. Behavior of Nanocelluloses at Interfaces. *Curr. Opin. Colloid Interface Sci.* **2017**, *29*, 83.

(22) Klemm, D.; Cranston, E. D.; Fischer, D.; Gama, M.; Kedzior, S. A.; Kralisch, D.; Kramer, F.; Kondo, T.; Lindström, T.; Nietzsche, S.; Petzold-Welcke, K.; Rauchfuß, F. Nanocellulose as a Natural Source for Groundbreaking Applications in Materials Science: Today's State. *Mater. Today* **2018**, *21*, 720.

(23) Yang, H.; Zhang, Y.; Kato, R.; Rowan, S. J. Preparation of Cellulose Nanofibers from Miscanthus x. Giganteus by Ammonium Persulfate Oxidation. *Carbohydr. Polym.* **2019**, *212*, 30−39.

(24) Weiss, A. M.; MacKe, N.; Zhang, Y.; Calvino, C.; Esser-Kahn, A. P.; Rowan, S. J. In Vitro and in Vivo Analyses of the Effects of Source, Length, and Charge on the Cytotoxicity and Immunocompatibility of Cellulose Nanocrystals. *ACS Biomater. Sci. Eng.* **2021**, *7* (4), 1450−1461.

(25) Li, W.; Ju, B.; Zhang, S. A Green L-Cysteine Modified Cellulose Nanocrystals Biosorbent for Adsorption of Mercury Ions from Aqueous Solutions. *RSC Adv.* **2019**, *9* (12), 6986−6994.

(26) Yu, X.; Tong, S.; Ge, M.; Wu, L.; Zuo, J.; Cao, C.; Song, W. Adsorption of Heavy Metal Ions from Aqueous Solution by Carboxylated Cellulose Nanocrystals. *J. Environ. Sci. (China)* **2013**, *25* (5), 933−943.

(27) Liu, P.; Sehaqui, H.; Tingaut, P.; Wichser, A.; Oksman, K.; Mathew, A. P. Cellulose and Chitin Nanomaterials for Capturing Silver Ions (Ag+) from Water via Surface Adsorption. *Cellulose* **2014**, *21* (1), 449−461.

(28) Sehaqui, H.; Perez de Larraya, U.; Tingaut, P.; Zimmermann, T. Humic Acid Adsorption onto Cationic Cellulose Nanofibers for Bioinspired Removal of Copper(Ii) and a Positively Charged Dye. *Soft Matter* **2015**, *11* (26), 5294−5300.

(29) Sheikhi, A.; Safari, S.; Yang, H.; van de Ven, T. G. M. Copper Removal Using Electrosterically Stabilized Nanocrystalline Cellulose. *ACS Appl. Mater. Interfaces* **2015**, *7* (21), 11301−11308.

(30) Saito, T.; Isogai, A. Ion-Exchange Behavior of Carboxylate Groups in Fibrous Cellulose Oxidized by the TEMPO-Mediated System. *Carbohydr. Polym.* **2005**, *61* (2), 183−190.

(31) Sehaqui, H.; de Larraya, U. P.; Liu, P.; Pfenninger, N.; Mathew, A. P.; Zimmermann, T.; Tingaut, P. Enhancing Adsorption of Heavy Metal Ions onto Biobased Nanofibers from Waste Pulp Residues for Application in Wastewater Treatment. *Cellulose* **2014**, *21* (4), 2831−2844.

(32) Shen, W.; Chen, S.; Shi, S.; Li, X.; Zhang, X.; Hu, W.; Wang, H. Adsorption of Cu(II) and Pb(II) onto Diethylenetriamine-Bacterial Cellulose. *Carbohydr. Polym.* **2009**, *75* (1), 110−114.

(33) Kardam, A.; Raj, K. R.; Srivastava, S.; Srivastava, M. M. Nanocellulose Fibers for Biosorption of Cadmium, Nickel, and Lead Ions from Aqueous Solution. *Clean Technol. Environ. Policy* **2014**, *16* (2), 385−393.

(34) Pillai, S. S.; Deepa, B.; Abraham, E.; Girija, N.; Geetha, P.; Jacob, L.; Koshy, M. Biosorption of Cd(II) from Aqueous Solution Using Xanthated Nano Banana Cellulose: Equilibrium and Kinetic Studies. *Ecotoxicol Environ. Saf* **2013**, *98*, 352−360.

(35) Liu, P.; Borrell, P. F.; Božič, M.; Kokol, V.; Oksman, K.; Mathew, A. P. Nanocelluloses and Their Phosphorylated Derivatives for Selective Adsorption of Ag+, Cu2+ and Fe3+ from Industrial Effluents. *J. Hazard Mater.* **2015**, *294*, 177−185.

(36) Ma, H.; Hsiao, B. S.; Chu, B. Ultrafine Cellulose Nanofibers as Efficient Adsorbents for Removal of UO22+ in Water. *ACS Macro Lett.* **2012**, *1* (1), 213−216.

(37) Batmaz, R.; Mohammed, N.; Zaman, M.; Minhas, G.; Berry, R. M.; Tam, K. C. Cellulose Nanocrystals as Promising Adsorbents for the Removal of Cationic Dyes. *Cellulose* **2014**, *21* (3), 1655−1665.

(38) Qiao, H.; Zhou, Y.; Yu, F.; Wang, E.; Min, Y.; Huang, Q.; Pang, L.; Ma, T. Effective Removal of Cationic Dyes Using Carboxylate-Functionalized Cellulose Nanocrystals. *Chemosphere* **2015**, *141*, 297−303.

(39) Timofei, S.; Schmidt, W.; Kurunczi, L.; Simon, Z. A Review of QSAR for Dye Affinity for Cellulose Fibres. *Dyes Pigm.* **2000**, *47* (1−2), 5−16.

(40) Dingenouts, N.; Patel, M.; Rosenfeldt, S.; Pontoni, D.; Narayanan, T.; Ballauff, M. Counterion Distribution around a Spherical Polyelectrolyte Brush Probed by Anomalous Small-Angle X-Ray Scattering. *Macromolecules* **2004**, *37* (21), 8152−8159.

(41) Patel, M.; Rosenfeldt, S.; Ballauff, M.; Dingenouts, N.; Pontoni, D.; Narayanan, T. Analysis of the Correlation of Counterions to Rod-like Macroions by Anomalous Small-Angle X-Ray Scattering. *Phys. Chem. Chem. Phys.* **2004**, *6* (11), 2962−2967.

(42) Das, R.; Mills, T. T.; Kwok, L. W.; Maskel, G. S.; Millett, I. S.; Doniach, S.; Finkelstein, K. D.; Herschlag, D.; Pollack, L. Counterion Distribution around DNA Probed by Solution X-Ray Scattering. *Phys. Rev. Lett.* **2003**, *90* (18), 188103.

(43) Pabit, S. A.; Finkelstein, K. D.; Pollack, L. Using Anomalous Small Angle X-Ray Scattering to Probe the Ion Atmosphere around Nucleic Acids. *Methods Enzymol* **2009**, *469*, 391−410.

(44) Pabit, S. A.; Meisburger, S. P.; Li, L.; Blose, J. M.; Jones, C. D.; Pollack, L. Counting Ions around DNA with Anomalous Small-Angle X-ray Scattering. *J. Am. Chem. Soc.* **2010**, *132* (46), 16334−16336.

(45) Pollack, L. SAXS Studies of Ion−Nucleic Acid Interactions. *Annu. Rev. Biophys.* **2011**, *40* (1), 225−242.

(46) Chen, J.; Bera, M. K.; Li, H.; Yang, Y.; Sun, X.; Luo, J.; Baughman, J.; Liu, C.; Yao, X.; Chuang, S. S. C.; Liu, T. Accurate Determination of the Quantity and Spatial Distribution of Counterions around a Spherical Macroion. *Angew. Chem., Int. Ed.* **2021**, *60* (11), 5833−5837.

(47) Sztucki, M.; di Cola, E.; Narayanan, T. Instrumental Developments for Anomalous Small-Angle X-Ray Scattering from Soft Matter Systems. *J. Appl. Cryst.* **2010**, *43* (6), 1479−1487.

(48) Stuhrmann, H. B. Anomalous Dispersion of Small-angle Scattering of Horse-spleen Ferritin at the Iron K Absorption Edge. *Acta Crystallogr., Sect. A* **1980**, *36* (6), 996−1001.

(49) Stuhrmann, H. B. Anomalous Small Angle Scattering. *Q. Rev. Biophys.* **1981**, *14* (3), 433−462.

(50) Stuhrmann, H. B.; Notbohm, H. Configuration of the Four Iron Atoms in Dissolved Human Hemoglobin as Studied by Anomalous Dispersion. *Proc. Natl. Acad. Sci. U. S. A.* **1981**, *78* (10), 6216.

(51) Tatchev, D. Structure Analysis of Multiphase Systems by Anomalous Small-Angle X-ray Scattering. *Philos. Mag.* **2008**, *88* (12), 1751−1772.

(52) Macke, N.; Hemmingsen, C. M.; Rowan, S. J. The Effect of Polymer Grafting on the Mechanical Properties of PEG-Grafted Cellulose Nanocrystals in Poly(Lactic Acid). *J. Polym. Sci.* **2022**, *60* (24), 3318−3330.

(53) Nagata, Y.; Mukamel, S. Electrical Double Layer Probed by Surface-Specific Vibrational Technique. *Chem.* **2018**, *4* (7), 1484−1485.

(54) Keshavarzi, E.; Abareghi, M. The Effect of Stern Layer Thickness on the Diffuse Capacitance for Size Asymmetric Electrolyte

inside the Charged Spherical Cavities by Density Functional Theory. *J. Electrochem. Soc.* **2022**, *169* (2), No. 020547.

(55) Brown, M. A.; Bossa, G. V.; May, S. Emergence of a Stern Layer from the Incorporation of Hydration Interactions into the Gouy-Chapman Model of the Electrical Double Layer. *Langmuir* **2015**, *31* (42), 11477−11483.

(56) *XModFit: X-ray Modeling and Fitting.* https://github.com/chemmatcars/XModFit (accessed 2023-02-21).

(57) Calero, C.; Faraudo, J.; Bastos-Gonz Alez, D. Interaction of Monovalent Ions with Hydrophobic and Hydrophilic Colloids: Charge Inversion and Ionic Specificity. *J. Am. Chem. Soc.* **2011**, *133*, 15025−15035.

(58) Yurtsever, A.; Wang, P.-X.; Priante, F.; Morais Jaques, Y.; Miyazawa, K.; MacLachlan, M. J.; Foster, A. S.; Fukuma, T. Molecular Insights on the Crystalline Cellulose-Water Interfaces via Three-Dimensional Atomic Force Microscopy. *Sci. Adv.* **2022**, *8* (41), eabq0160.

(59) Zhang, Y.; Yang, H.; Naren, N.; Rowan, S. J. Surfactant-Free Latex Nanocomposites Stabilized and Reinforced by Hydrophobically Functionalized Cellulose Nanocrystals. *ACS Appl. Polym. Mater.* **2020**, *2* (6), 2291−2302.

(60) Malaspina, D. C.; Faraudo, J. Molecular Insight into the Wetting Behavior and Amphiphilic Character of Cellulose Nano-crystals. *Adv. Colloid Interface Sci.* **2019**, *267*, 15−25.

(61) Gestranius, M.; Stenius, P.; Kontturi, E.; Sjöblom, J.; Tammelin, T. Phase Behaviour and Droplet Size of Oil-in-Water Pickering Emulsions Stabilised with Plant-Derived Nanocellulosic Materials. *Colloids Surf. A Physicochem Eng. Asp* **2017**, *519*, 60−70.

(62) Kalashnikova, I.; Bizot, H.; Cathala, B.; Capron, I. Modulation of Cellulose Nanocrystals Amphiphilic Properties to Stabilize Oil/Water Interface. *Biomacromolecules* **2012**, *13* (1), 267−275.

(63) Giles, C. H.; MacEwan, T. H.; Nakhwa, S. N.; Smith, D. Studies in adsorption. Part XI. A System of Classification of Solution Adsorption Isotherms, and Its Use in Diagnosis of Adsorption Mechanisms and in Measurement of Specific Surface Areas of Solids. *J. Chem. Soc.* **1960**, 3973−3993.

(64) Piccin, J. S.; Cadaval, T. R. S. A.; De Pinto, L. A. A.; Dotto, G. L. Adsorption Isotherms in Liquid Phase: Experimental, Modeling, and Interpretations. *Adsorption Processes for Water Treatment and Purification* **2017**, 19−51.

(65) Sexsmith, F. H.; White, H. J. The Absorption of Cationic Surfactants by Cellulosic Materials: I. The Uptake of Cation and Anion by a Variety of Substrates. *J. Colloid Sci.* **1959**, *14* (6), 598−618.

(66) Sexsmith, F. H.; White, H. J. The Absorption of Cationic Surfactants by Cellulosic Materials: III. A Theoretical Model for the Absorption Process and a Discussion of Maxima in Absorption Isotherms for Surfactants. *J. Colloid Sci.* **1959**, *14* (6), 630−639.

(67) *X-ray Anomalous Scattering (XAnoS).* https://github.com/nayanbera/XAnoS (accessed 2023-02-21).

(68) Bera, M. K.; Bu, W. *XModFit: X-Ray Modeling and Fitting,* Zenodo, 2022. https://zenodo.org/records/7047225.

(69) Ilavsky, J.; Jemian, P. R. *Irena*: tool suite for modeling and analysis of small-angle scattering. *J. Appl. Cryst.* **2009**, *42*, 347−353.